A&A 488, 959–968 (2008)
DOI: 10.1051/0004-6361:200809673

Astronomy
&
Astrophysics

An interferometric study of the low-mass protostar IRAS 16293-2422: small scale organic chemistry[⋆]

S. E. Bisschop[1,⋆⋆], J. K. Jørgensen[2], T. L. Bourke[3], S. Bottinelli[1], and E. F. van Dishoeck[1,4]

[1] Leiden Observatory, Leiden University, PO Box 9513, 2300 RA Leiden, The Netherlands
e-mail: `bisschop@mpifr-bonn.mpg.de`
[2] Argelander-Institut für Astronomie, University of Bonn, Auf dem Hügel 71, 53121 Bonn, Germany
[3] Harvard-Smithsonian Center for Astrophysics, 60 Garden Street, Cambridge, MA 02138, USA
[4] Max-Planck-Institut für Extraterrestische Physik, Giessenbachstrasse 1, 85748 Garching, Germany

Received 28 February 2008 / Accepted 9 July 2008

ABSTRACT

Aims. We investigate the chemical relations between complex organics based on their spatial distributions and excitation conditions in the low-mass young stellar objects IRAS 16293-2422 "A" and "B".
Methods. Interferometric observations with the Submillimeter Array have been performed at $5'' \times 3''$ (800×500 AU) resolution revealing emission lines of HNCO, CH_3CN, CH_2CO, CH_3CHO and C_2H_5OH. Rotational temperatures are determined from rotational diagrams when a sufficient number of lines are detected.
Results. Compact emission is detected for all species studied here. For HNCO and CH_3CN it mostly arises from source "A", CH_2CO and C_2H_5OH have comparable strength for both sources and CH_3CHO arises exclusively from source "B". HNCO, CH_3CN and CH_3CHO have rotational temperatures >200 K implying that they arise from hot gas. The (u, v)-visibility data reveal that HNCO also has extended cold emission, which could not be previously determined through single dish data.
Conclusions. The relative abundances of the molecules studied here are very similar within factors of a few to those found in high-mass YSOs. This illustrates that the chemistry between high- and low-mass objects appears to be relatively similar and thus independent of luminosity and cloud mass. In contrast, bigger abundance differences are seen between the "A" and "B" source. For instance, the HNCO abundance relative to CH_3OH is ~4 times higher toward "A", which may be due to a higher initial OCN^- ice abundances in source "A" compared to "B". Furthermore, not all oxygen-bearing species are co-existent, with CH_3CHO/CH_3OH an order of magnitude higher toward "B" than "A". The different spatial behavior of CH_2CO and C_2H_5OH compared with CH_3CHO suggests that successive hydrogenation reactions on grain-surfaces are not sufficient to explain the observed gas phase abundance of the latter. Selective destruction of CH_3CHO may result in the anti-coincidence of these species in source "A". These results illustrate the power of interferometric compared with single dish data in terms of testing chemical models.

Key words. astrochemistry – line: identification – methods: observational – techniques: interferometric – stars: formation

1. Introduction

The envelopes of some low-mass protostars contain many complex organic molecules[1] (Blake et al. 1994; van Dishoeck et al. 1995; Cazaux et al. 2003; Bottinelli et al. 2004a,b, 2007b; Jørgensen et al. 2005a,b; Sakai et al. 2006, 2007). This raises the question whether these are low-mass versions of "hot cores", chemically very rich environments in high-mass star forming regions that are thought to have their origin in grain-mantle evaporation and the subsequent rapid gas phase reactions. The low-mass counterpart is sometimes called a "hot corino". The presence of warm material has long been suggested from modeling of the SEDs of these sources (e.g., Adams et al. 1987; Jørgensen et al. 2002; Shirley et al. 2002) and has been firmly established by molecular excitation studies (Blake et al. 1994; van Dishoeck et al. 1995; Ceccarelli et al. 2000) and by resolved interferometric imaging (see e.g., Chandler et al. 2005; Bottinelli et al. 2004b; Jørgensen et al. 2005c). However, in some sources the emission peaks offset from the continuum source (e.g., Chandler et al. 2005). This offset is in disagreement with the "hot corino" hypothesis for low-mass stars in which complex molecules evaporate through passive heating and is more in favor of other explanations such as the presence of disks or outflows that create shocks in the envelope. Currently, there is an ongoing debate on whether the emission of complex organics comes from "hot corinos" or from other types of regions. Also, the extent to which the observed organics are first generation molecules created in the ice or second generation produced in the gas is still an open question. The aim of this work is to map the emission of complex organics to address the latter question, namely to determine their most likely formation mechanism.

One method to study chemical links between species is to study molecular abundances through single-dish surveys in a large number of sources (van der Tak et al. 2000, 2003; Ikeda et al. 2001; Bisschop et al. 2007b). An alternative method is to look for spatial correlations by interferometric observations of a single source through which it is possible to distinguish compact and extended emission as well as the exact location of the compact emission. The species that are studied here are the nitrogen-bearing species, HNCO and CH_3CN and the

---

[⋆] Appendix A is only available in electronic form at `http://www.aanda.org`
[⋆⋆] *Current address*: Max-Planck-Institut für Radioastronomie, Auf dem Hügel 69, 53121 Bonn, Germany.
[1] In this paper molecules are considered complex if they contain more than four atoms.

Table 1. Line parameters and fluxes from detected HNCO and CH_3CN transitions for the "A" and "B" components. The figures in which the lines are shown are indicated in the last column.

Molecule	Freq.	Transition	E_u	μ^2S	$F\Delta V^a$ (Jy km s^{-1}) [σ]		Figure
	(GHz)		(K)	(D^2)	"A"	"B"	
HNCO	219.657	$10_{3,7/8}-9_{3,6/7}$	447	139.2	4.9 [22σ]	0.54 [8σ]	A.1
	219.733	$10_{2,9}-9_{2,8}$	231	73.8	10.5^b [41σ]	0.37 [6σ]	A.1
	219.737	$10_{2,8}-9_{2,7}$	231	73.8	10.5^b [41σ]	0.30 [5σ]	A.1
	219.798	$10_{0,10}-9_{0,9}$	58	77.0	10.9 [49σ]	1.37 [12σ]	1
	220.584	$10_{1,9}-9_{1,8}$	102	76.2	9.6 [43σ]	1.19 [13σ]	3
CH_3CN	220.476	12_8-11_8	526	608.6	2.4 [11σ]	0.45 [7σ]	A.1
	220.539	12_7-11_7	419	722.8	3.1 [14σ]	0.44 [7σ]	A.1
	220.594	12_6-11_6	326	1643.3	$-^c$	1.56 [14σ]	3
	220.641	12_5-11_5	247	905.3	$-^d$	1.81 [19σ]	3
	220.679	12_4-11_4	183	973.9	11.4 [52σ]	1.76 [19σ]	A.2
	220.709	12_3-11_3	133	2054.4	14.8 [67σ]	2.21 [23σ]	A.2
	220.730	12_2-11_2	97	1065.1	14.3 [65σ]	2.07 [22σ]	A.2
	220.742	12_1-11_1	76	1088.0	$-^d$	2.23 [24σ]	A.2
	220.747	12_0-11_0	69	1095.6	$-^d$	2.47 [26σ]	1, A.2
$CH_3^{13}CN$	220.600	12_3-11_3	133	2066.3	$-^d$	0.88 [9σ]	3
	220.621	12_2-11_2	97	1071.4	$-^d$	0.69 [7σ]	3
	220.634	12_1-11_1	76	1094.4	$-^d$	0.61 [6σ]	3
	220.638	12_0-11_0	69	1102.1	$-^d$	0.44 [5σ]	3

[a] $F\Delta V$ is determined over the full width of the emission coming from source "A" or "B", respectively. [b] The $10_{2,9}-9_{2,8}$ and $10_{2,8}-9_{2,7}$ transitions for HNCO are blended in source "A". The flux given is the total combined flux for both lines. [c] Blended with the C_2H_5OH $13_{1,13}-12_{0,12}$ transition. [d] Strongly blended lines.

oxygen-bearing species CH_2CO, CH_3CHO, and C_2H_5OH that are commonly found toward or surrounding hot cores. The molecules CH_2CO, CH_3CHO and C_2H_5OH are proposed to be linked by successive hydrogenation on the surfaces of grains (Tielens & Charnley 1997).

The source studied in this paper, IRAS 16293-2422, is a very well studied and chemically rich low-mass YSO. It is a binary with its main components, named "A" and "B", separated by 5″ (corresponding to 800 AU at 160 pc Mundy et al. 1992). From single dish observations and modeling, van Dishoeck et al. (1995), Ceccarelli et al. (1999, 2000) and Schöier et al. (2002) concluded that emission from several organic molecules arises from a compact region. The data for some species such as H_2CO and CH_3CN are significantly better fitted if a "jump" in the abundance at 80−90 K due to grain-mantle evaporation is assumed in a spherical circum-binary envelope (Ceccarelli et al. 2000; Schöier et al. 2002). Through interferometric observations it is possible to distinguish between the emission from the cold extended envelope and more compact emission as well as the peak location: is the emission coming from source "A" or "B"? Previous observations have shown that some complex species are much more abundant toward one source than the other, such as CH_3OCHO which is more prominent toward the "A" source (Bottinelli et al. 2004b; Huang et al. 2005; Kuan et al. 2004; Remijan & Hollis 2006).

The nitrogen-bearing species HNCO and CH_3CN have previously been detected toward IRAS 16293-2422 through single dish observations (van Dishoeck et al. 1995; Cazaux et al. 2003). They often have high rotational temperatures in star forming regions implying that they are present in hot gas (Olmi et al. 1993; Zinchenko et al. 2000; Cazaux et al. 2003; Bisschop et al. 2007b). This is also the case for the oxygen-bearing molecule C_2H_5OH (Ikeda et al. 2001; Bisschop et al. 2007b). In contrast, CH_2CO and CH_3CHO are often detected in high-mass sources with low rotational temperatures (Ikeda et al. 2002; Bisschop et al. 2007b). For CH_3CHO higher rotational temperatures are also found, but these can be due to the b-type transitions that are radiatively pumped and do not represent the actual kinetic temperature of the gas (Nummelin et al. 2000; Turner 1991). Recent laboratory experiments by Bisschop et al. (2007a) have shown that it is possible to explain the gas phase abundances of C_2H_5OH if a solid state formation route through CH_3CHO hydrogenation is assumed. The observed absence of CH_3CHO in hot gas combined with its detection in cold ices (Keane 2001; Gibb et al. 2004), however, implies that it must be destroyed at higher ice temperatures, before evaporation commences, or directly after evaporation in the gas phase. A comparison of the excitation properties as well as interferometric observations in which the spatial distribution of the species can be determined are good tools to further elucidate the chemical relations between these species.

This paper is structured as follows: Sect. 2 presents the Submillimeter Array (SMA) observing strategy as well as maps and spectra; Sect. 3 explains the analysis of the interferometric observations in the (u, v)-plane and the fitting of rotational diagrams; Sect. 4 presents the results of the rotational diagram and flux analysis; Sect. 5 discusses the relative abundances of the different species with respect to each other as well as the implications for the chemistry; Sect. 6 summarizes the main conclusions.

2. Observations

2.1. Observing strategy

The line-rich low-mass protostar, IRAS 16293-2422, at a distance of 160 pc, has been surveyed from 2004 to 2005 using the Submillimeter Array[2] (SMA) in a large number of frequency settings. In this paper we focus on just the emission lines from HNCO, CH_3CN, C_2H_5OH, CH_2CO and CH_3CHO for which

---

[2] The Submillimeter Array is a joint project between the Smithsonian Astrophysical Observatory and the Academia Sinica Institute of Astronomy and Astrophysics. It is funded by the Smithsonian Institute and Academia Sinica.

Table 2. Line parameters and fluxes from detected CH_2CO, CH_3CHO and C_2H_5OH transitions for the "A" and "B" components. The figures in which the lines are shown are indicated in the last column.

Molecule	Freq. (GHz)	Transition	E_u (K)	$\mu^2 S$ (D^2)	$F\Delta V^a$ (Jy km s^{-1}) [σ] "A"	"B"	Figure
CH_2CO	220.178	$11_{1,11}-10_{1,10}$	76	65.4	3.98 [18σ]	3.30 [35σ]	1
CH_3CHO-A^b	219.780	$11_{1,10}-10_{1,9}$	435	66.4	<0.22	0.43 [7σ]	A.3
	230.302	$12_{2,11}-11_{2,10}$	81	73.7	<0.22	2.23 [24σ]	A.3
	230.395	$12_{2,11}-11_{2,10}$	286	74.1	<0.22	1.01 [17σ]	A.3
	230.438	$12_{0,12}-11_{0,11}$	440	72.9	<0.22	0.66 [8σ]	A.3
	231.330	$12_{5,8/7}-11_{5,7/6}$	129	125.5	<0.22	2.66 [28σ]	A.3
CH_3CHO-E^b	231.357	$12_{3,9}-11_{3,8}$	299	71.4	<0.22	1.32 [14σ]	A.4
	231.363	$12_{5,7}-11_{5,6}$	129	62.7	<0.22	2.44 [26σ]	A.4
	231.369	$12_{5,8}-11_{5,7}$	129	62.7	<0.22	1.94 [21σ]	A.4
C_2H_5OH	220.602	$13_{1,13}-12_{0,12}$	74	44.7	–^{c}	4.02 [34σ]	1, 3, 4

^{a} $F\Delta V$ is determined over the full width of the emission coming from source "A" or "B", respectively. ^{b} 3σ upper limits are calculated assuming that the CH_3CHO-A and E lines have the same line-widths as CH_2CO. ^{c} Blended with the $CH_3^{13}CN$ 12_3-11_3 and CH_3CN 12_6-11_6 transitions.

particularly sensitive data exist (see Tables 1 and 2). Other papers presenting data from this survey are Takakuwa et al. (2007) and Yeh et al. (2008).

The data shown here were all covered in one spectral setup at 219.4–221.3 GHz (LSB) and 229.4–231.3 GHz (USB) on February 18th 2005 with 6 antennas in the compact configuration of the array, resulting in 15 baselines from 10–70 m. This frequency setup was chosen to complement a large SMA survey of Class 0 sources (Jørgensen et al. 2007) and includes, e.g., the strong CO transitions and its isotopologues and a large number of lines from organic molecules. The data were taken as part of dual receiver observations simultaneously with high frequency 690 GHz data (Bourke et al., in prep.). The weather was optimal for the 690 GHz observations with $\tau_{225\ \mathrm{GHz}}$ better than 0.03. The excellent weather conditions and the dual receiver option naturally provides a possibility for very high quality observations at the lower frequencies. The overall flux calibration is estimated to be 30%. The phase center for the observations, $(\alpha, \delta)_{\mathrm{J2000}}$ = (16:32:22.9, −24:28:35.5), is located about 1″ to the north from the "A" component of the IRAS 16293-2422 binary. The synthesized beam was 5.5″ × 3.2″, which corresponds to 800 × 500 AU at 160 pc. The SMA correlator was set up with uniform coverage of the 2 GHz bandwidth with 128 channels for each of the 24 chunks, corresponding to a spectral resolution of 1.1 km s^{-1}. The RMS was 60 mJy $beam^{-1}$ $channel^{-1}$.

The initial data reduction was performed using the MIR package (Qi 2006). The complex gains were calibrated by frequent observations of the quasar J1743-038 (3.0 Jy) offset by 27 degrees from IRAS 16293-2422. Flux and band-pass calibration was performed by observations of Uranus. Continuum subtracted line maps and further analysis were subsequently made using the Miriad package.

2.2. Maps and spectra

Figure 1 displays the maps and selected spectra toward the "A" and "B" components of IRAS 16923-2422, whereas the spectra of additional lines are shown in Figs. 1, 3, 4 and the online Appendix A in Figs. A.1–A.4 (see also Tables 1 and 2). The line identifications are based on comparison with the CDMS[3], JPL[4] and NIST[5] catalogs. The assignments are assumed to be secure when no other species emits close to the observed frequency. Note that for CH_3CHO the frequencies from the NIST catalog have been used, because the data in the JPL catalog are based on extrapolations of the line positions from lower frequencies. These are shifted by a few MHz or more from the actual measured line positions in the laboratory by Kleiner et al. (1996).

From Fig. 1 it is clear that significant physical differences exist between the regions where the emission from these two sources arises. As previously noted by Bottinelli et al. (2004b) and Kuan et al. (2004) the spectra toward "A" show broad lines with a *FWHM* of 8 km s^{-1}, whereas the lines toward "B" are much narrower, typically less than 2 km s^{-1} wide (~2 channels). The high excitation lines of the complex organics peak at V_{LSR} = 1.5–2.5 km s^{-1} toward both sources. This is in contrast to the systemic velocities of the larger scale envelope, e.g., traced by HCN, at 3–4.5 km s^{-1} (Takakuwa et al. 2007). The maps displayed in Fig. 1 are obtained by integrating over the width of the "B" component. Since the line-width in source "A" is much larger and the peak intensity is much lower than that of source "B", only a fraction of the total flux of the CH_2CO line in source "A" is shown in the maps in Fig. 1 (see also Table 2). When the CH_2CO line is integrated over the line-width from source "A" of 8 km s^{-1} equally strong peaks for both sources are detected as is illustrated in Fig. 2, where the maps for CH_2CO are shown integrated over both velocity ranges.

HNCO and CH_3CN show much weaker emission at the "B" position, i.e., 8% and 18% respectively of that at the "A" position whereas CH_3CHO is only seen toward the "B" position. Tables 1 and 2 list the integrated line intensities for positions "A" and "B". When there is no detection, 3σ upper limits to the intensity are given provided that there is no overlap with other species. Lines of isotopologues were also searched to check the optical depth. No $HN^{13}CO$ lines were detected leading to a lower limit for HNCO/$HN^{13}CO$ of about 10. Since even high-mass objects show no evidence for high optical depth (Zinchenko et al. 2000; Bisschop et al. 2007b), we assume for the remainder of this paper that the emission from HNCO is optically thin. $CH_3^{13}CN$ is clearly detected toward source "B" as is shown in Fig. 3 for the $CH_3^{13}CN$ branch. The $CH_3^{13}CN$ transitions (see Fig. 3) are strongly blended in source "A". However, it is probable that it is present since there is emission toward source "A" that coincides with the locations of the $CH_3^{13}CN$ transitions. Due to the

---

[3] `http://www.astro.uni-koeln.de/cdms/`

[4] `http://spec.jpl.nasa.gov/ftp/pub/catalog/catform.html`

[5] `http://physics.nist.gov/cgi-bin/micro/table5/start.pl`

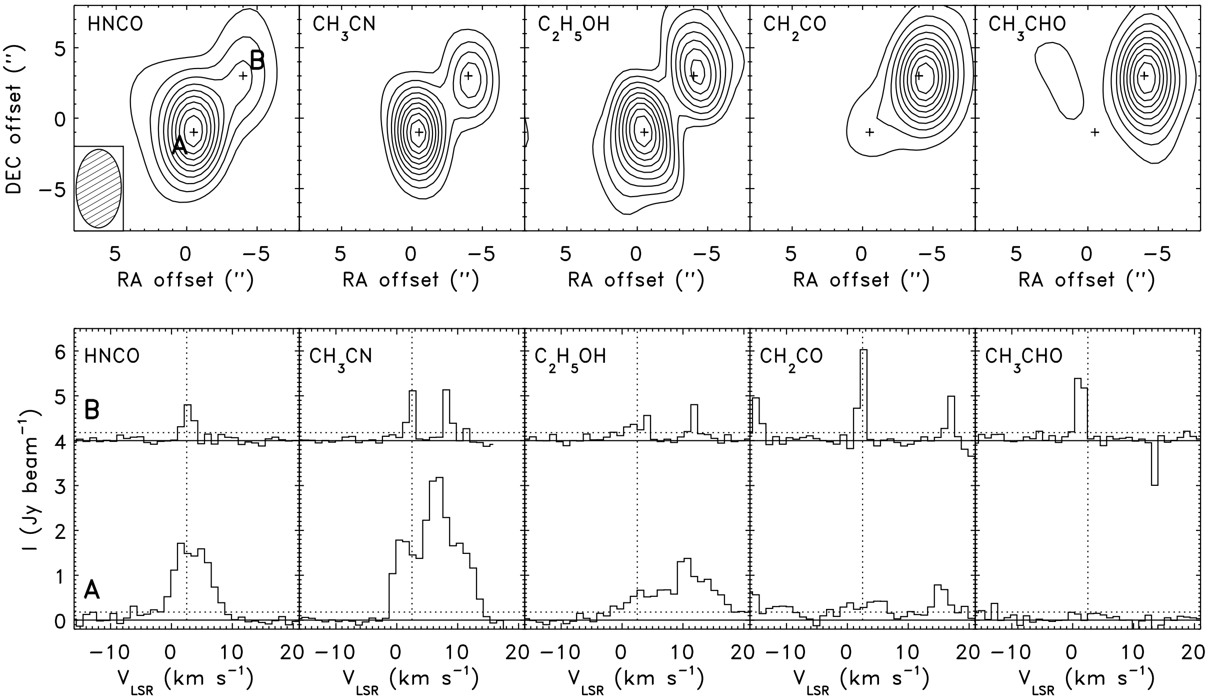

Fig. 1. Maps and spectra of the HNCO $10_{0,10}-9_{0,9}$, CH_3CN 12_0-11_0, C_2H_5OH $13_{1,13}-12_{0,12}$, CH_2CO $11_{1,11}-10_{1,10}$ and CH_3CHO $12_{5,8/7,0}-11_{5,7/6,0}$ lines from −15–20 km s^{-1}. The maps (*upper panels*) show the emission integrated over the width of the "B" component i.e. ±1.0–1.5 km s^{-1} around the systemic velocity. The contour levels are at 10%, 20%, etc. of the peak in the maps. The peak integrated intensities are 10.3, 3.5, 1.0, 3.2, 2.7 Jy km s^{-1} for HNCO, CH_3CN, C_2H_5OH, CH_2CO and CH_3CHO, respectively. The size of the SMA beam is indicated in the lower left corner of the HNCO map for comparison. In the spectra (*lower panels*) the lower row indicates the spectra toward "A" and the upper row toward "B" shifted in the vertical scale by 4 Jy beam^{-1}. A dotted vertical line at $\upsilon_{LSR} = 2$ km s^{-1} indicates the average systemic velocity for the compact emission toward "A" and "B". The additional emission feature present at 8 km s^{-1} next to CH_3CN 12_0-11_0 is the CH_3CN 12_1-11_1 transition and that next to CH_2CO $11_{1,11}-10_{1,10}$ is the $HCOOCH_3$ $17_{2,15}-16_{4,12}$ transition. Note that small velocity differences are present between the sources and perhaps even between different species. Solid and dashed horizontal lines indicate the baseline and the 3σ level per channel, respectively.

line-blends, it is unfortunately not possible to determine accurate integrated line-intensities for source "A". For source "B", however, they can be determined. The $CH_3CN/CH_3^{13}CN$ ratio is ∼10 with a relatively large uncertainty on the fluxes of 40% due to the low signal-to-noise. The $CH_3CN/CH_3^{13}CN$ ratio is much lower than the $^{12}C/^{13}C$ ratio of 77 ± 7 determined by Wilson & Rood (1994) for the local ISM and the estimated optical depth is ≈2. The CH_3CN emission for "A" is probably optically thick as well. A high optical depth toward IRAS 16293-2422 for CH_3CN was also found by Bottinelli et al. (2004b). Note that for high optical depth the rotation temperature and number of molecules derived from the rotation diagram will be upper and lower limits, respectively.

The C_2H_5OH $13_{1,13}-12_{0,12}$ transition is detected toward source "B" shown in Figs. 3 and 4. It is strongly blended with the $CH_3^{13}CN$ 12_3-11_3 transition at 220.600 GHz, and for source "A" also with the CH_3CN 12_6-11_6 transition at 220.594 GHz. This makes the estimate of the number of molecules from this line very uncertain, even though it is detected and the identification of the line seems secure for source "B".

3. Analysis

3.1. Disentangling compact and extended emission: fits in the (u, v)-plane

One of the issues in dealing with interferometric observations of protostars is that a significant fraction of the emission may be resolved out, especially for low excitation transitions of molecules also present in the large scale cold envelopes. Furthermore, fits in the image plane suffer from the effects of the Fourier transformation and image deconvolution, in particular for sparsely sampled data.

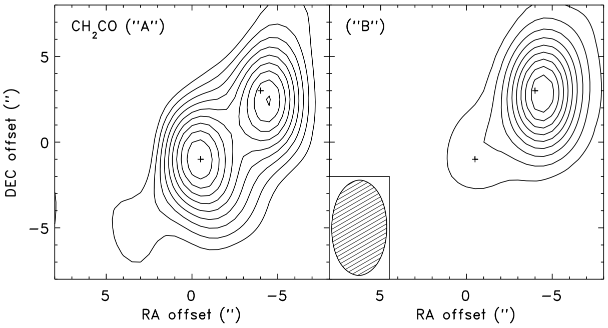

Fig. 2. Maps for the CH_2CO $11_{1,11}-10_{1,10}$ line integrated over the width of the "A" component of ±4 km s^{-1} (*left*) and "B" component of ±1–1.5 km s^{-1} (*right*) around the systemic velocity. The size of the SMA beam is shown in the map of the "B" component for comparison.

We have analyzed the data directly in the (u, v)-plane of the interferometric observations to investigate the molecular emission as function of baseline length, where longer baselines correspond to more compact emission, and compared this to the single dish flux measured by the JCMT. Figure 5 illustrates this for the lowest excitation HNCO $10_{0,10}-9_{0,9}$ line at 219.798 GHz (E_u = 58 K). These observations show a break around 15 kλ (2000 AU) with an almost constant amplitude at longer baselines, implying that there is an additional compact (unresolved) component contributing to the emission. This break is consistent

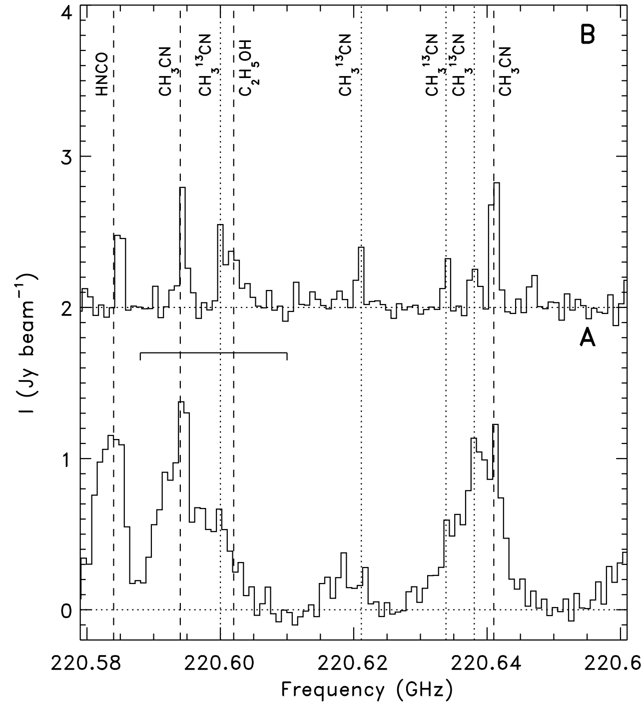

Fig. 3. SMA spectrum in the 220.580–220.66 GHz range for sources "A" (*lower spectrum*) and "B" (*upper spectrum*). The dotted lines indicate from left to right the positions of the 12_3-11_3, 12_2-11_2, 12_1-11_1 and 12_0-11_0 $CH_3^{13}CN$ transitions and the dashed lines the positions of lines for other species, in particular the $10_{1,9}-9_{1,8}$ HNCO, 12_6-11_6 and 12_5-11_5 CH_3CN and $13_{1,13}-12_{0,12}$ C_2H_5OH transitions. The frequency range shown in more detail in Fig. 4 is indicated with a bar above the spectrum of source "A". Note that the x-axis here is given in GHz and in Fig. 4 in km s^{-1}, so that the spectra are reversed compared to each other. The horizontal dotted lines show the baseline.

with the analysis of single dish data by Schöier et al. (2002), which gives an abundance enhancement in the innermost envelope. For shorter baselines the flux increases and the single dish flux with the JCMT is recovered within the uncertainty. When the analysis is restricted to the longer baselines, the emission can be compared for compact emission exclusively without worrying about the presence of extended envelope material. For all other lines and species the point source fits are therefore made to baselines longer than 17 kλ integrated over the velocity range of each component. This results in the fluxes listed in Tables 1 and 2. For the HNCO $10_{0,10}-9_{0,9}$ transition, about a third of the flux is observed at the longest baselines, due to compact emission, whereas the remaining two thirds can be attributed to the extended cold envelope. This is the only species, however, where a significant increase is seen for shorter baselines. Thus, most of the emission from the remaining species is unresolved although colder extended material is not excluded (see Sect. 4).

3.2. Rotational diagrams

When multiple transitions of a given molecule are observed spanning a large range in excitation energies it is possible to infer the physical properties of the emitting gas under various assumptions. The rotational diagram method (e.g., Goldsmith & Langer 1999) is often used for molecules of different excitation energies. Under the assumption that the emitting gas is optically thin a straightforward relationship exists between the integrated intensities, the column density of the molecule and its so-called "rotational temperature". At high densities this will approach the kinetic temperature of the gas.

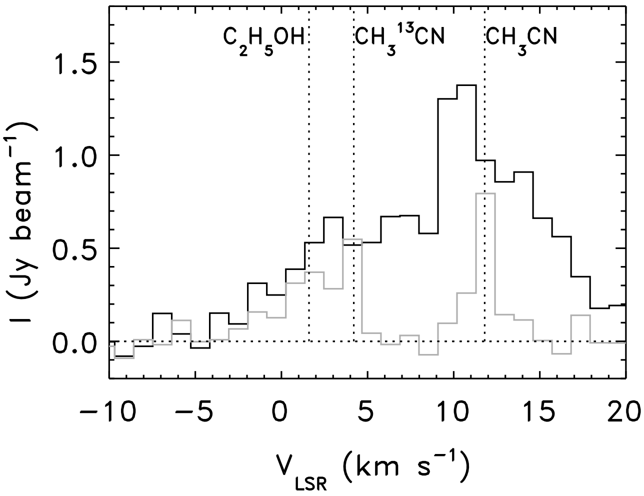

Fig. 4. SMA spectrum of the C_2H_5OH $13_{1,13}-12_{0,12}$ line at 220.602 GHz (dotted line at 2.5 km s^{-1}). The black line indicates the emission spectrum toward "A" and the grey line toward "B". The dotted vertical lines indicate the position of the $CH_3^{13}CN$ 12_3-11_3 transition at 220.600 GHz (4 km s^{-1}) and the CH_3CN 12_6-11_6 transition at 220.594 GHz (12.5 km s^{-1}) assuming their emission arises at υ_{LSR} = 2 km s^{-1}. The horizontal dotted line shows the baseline.

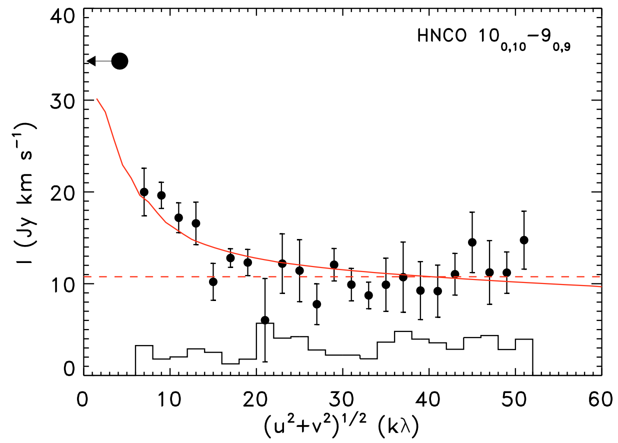

Fig. 5. Visibility amplitudes of the emission for the HNCO $10_{0,10}-9_{0,9}$ transition at 219.798 GHz observed with the SMA as a function of the projected interferometric baseline length with the phase center taken at 1″ north of the "A" component. The large filled circle near 35 km s^{-1} indicates the flux detected for the same line with the JCMT. The solid line represents a fit to the flux at different baselines using the Schöier et al. (2002) model and assuming a "jump" in the abundance for HNCO at 90 K. The dashed line corresponds to the average visibility amplitude for baselines longer than 17 kλ. The histogram gives the expected amplitude for zero observed signal, i.e., in the absence of source emission.

For single-dish observations one typically assumes that the source is compact with respect to the beam and that a specific beam filling factor (or source size) applies as a correction to the observed intensities. For the interferometric observations presented here we know that the source is unresolved at a specific angular resolution. It is therefore more natural to work directly in units of flux densities, so that the analysis is independent of an unknown source size. For an optically thin source, ignoring

Table 3. Rotational temperature, $T_{\rm rot}$, total number of molecules, $Y_{\rm T}$, and abundance with respect to HNCO, $x_{\rm HNCO}$.

Molecule	Source "A"			Source "B"		
	$T_{\rm rot}$ (K)	$Y_{\rm T}^{a}$ (mol.)	$x_{\rm HNCO}$	$T_{\rm rot}$ (K)	$Y_{\rm T}^{a}$ (mol.)	$x_{\rm HNCO}$
HNCO	277±76	8.9(14)	1.0	237±56	7.5(13)	1.0
CH_3CN^b	<372±110	≥5.6(14)	>0.6	<390±99	$1.1(15)^c$	14
$CH_3^{13}CN$	–	–	–	261±485	$1.4(13)^c$	0.19
CH_2CO^d	–	5.6(14)	0.6	–	4.7(14)	6.3
CH_3CHO	–	$<2.2(13)^e$	$<0.02^e$	250±49	3.2(14)	4.3
$C_2H_5OH^d$	–	–	–	–	7.1(14)	9.5

[a] The notation $y(z)$ stands for $y \times 10^z$. [b] $T_{\rm rot}$ for CH_3CN in both sources is calculated assuming the main isotope is optically thin, and is therefore an upper limit (see Sect. 3.2), whereas $Y_{\rm T}$ is a lower limit. [c] $Y_{\rm T}$ for CH_3CN and $CH_3^{13}CN$ in source "B" has been determined from the $CH_3^{13}CN$ lines assuming a $^{12}C/^{13}C$ ratio of 77 (Wilson & Rood 1994). [d] $Y_{\rm T}$ for CH_2CO and C_2H_5OH in source "B" are derived assuming they have the same rotational temperature as CH_3CHO (see Table 2). [e] The upper limit is derived for CH_3CHO toward source "A" with the assumption that the rotational temperature is identical to that in source "B".

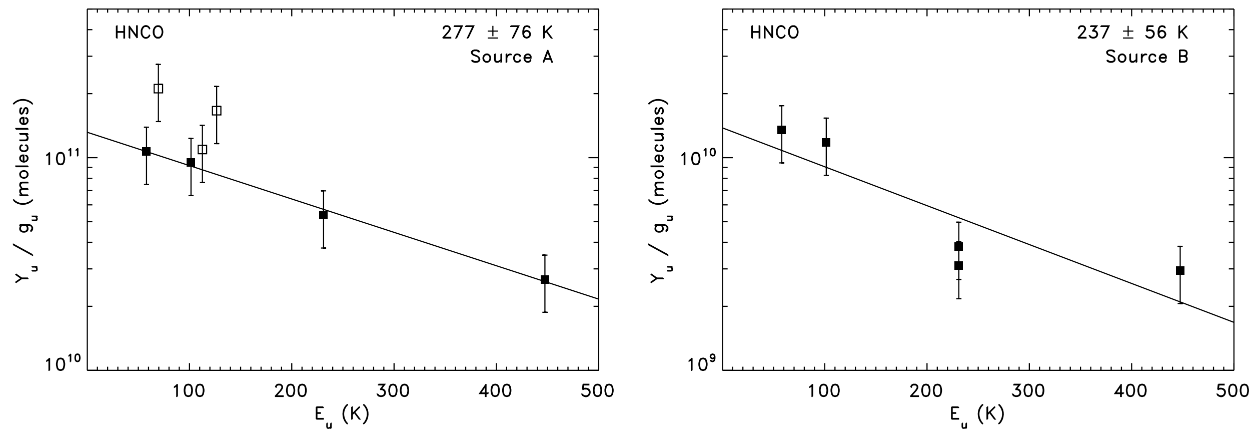

Fig. 6. Rotational diagram for HNCO transitions detected with the SMA shown as filled squares (■) toward sources "A" (*left panel*) and "B" (*right panel*). Emission lines detected with the single dish telescopes JCMT and CSO by van Dishoeck et al. (1995) are indicated with open squares (□), but are not used for the fit. Uncertainties of 30% are over-plotted on the data.

background radiation, the source brightness at a specific frequency, I_ν is then given by:

$$I_\nu = \frac{A_{\rm ul} N_{\rm u}^{\rm thin} hc}{4\pi\Delta V}, \tag{1}$$

where $A_{\rm ul}$ is the Einstein coefficient, $N_{\rm u}^{\rm thin}$ the column density of molecules in the upper energy level and ΔV the emission linewidth. Assuming the source emits uniformly over a solid angle, Ω, we can also express the column density $N_{\rm u}^{\rm thin}$ as the total number of molecules, $Y_{\rm u}^{\rm thin} = N_{\rm u}^{\rm thin}\Omega$. Since the definition of brightness of a uniform source is $I_\nu = S_\nu/\Omega$ where S_ν is the flux density, we can write:

$$S_\nu = \frac{A_{\rm ul} Y_{\rm u}^{\rm thin} hc}{4\pi\Delta V} \cdot \tag{2}$$

Note that in contrast to the typical calculation for rotational diagrams, the source size does not enter the equation here – only the total number of molecules. The observed quantity from this expression is the integrated line intensity, $S_\nu\Delta V$, typically measured in Jy km s^{-1}.

From this expression it is straightforward to isolate the number of molecules in the energy level, $Y_{\rm u}^{\rm thin}$, and through the Boltzmann equation relate it to the total number of molecules, $Y_{\rm T}$:

$$\frac{Y_{\rm u}^{\rm thin}}{g_{\rm u}} = \frac{Y_{\rm T}}{Q(T_{\rm rot})} {\rm e}^{-E_{\rm u}/T_{\rm rot}}, \tag{3}$$

where $g_{\rm u}$ is the degeneracy of the upper energy level, Q the molecular partition function, $T_{\rm rot}$ the rotational temperature and $E_{\rm u}$ the energy of the upper energy level. As in the usual rotational diagram analysis, one can then plot $Y_{\rm u}^{\rm thin}/g_{\rm u}$ versus $E_{\rm u}$, and derive the rotational temperature, $T_{\rm rot}$, from the slope and the total number of molecules, $Y_{\rm T}$, from the interpolation to $E_{\rm u} = 0$ K. Column densities can be derived for interferometric observations but as for the single-dish observations an assumption for source size has to be made.

In this way rotational diagrams were fit for all molecules with a sufficient number of detected lines. The results are summarized in Table 3. For some species no rotational temperature could be determined, since too few lines were detected. In that case $Y_{\rm T}$ is derived assuming that these species have the same rotational temperature as other chemically related species in the same source. In Sect. 4 we discuss these results in detail for each molecule.

4. Results

4.1. HNCO and CH_3CN

The rotational diagrams for HNCO are shown in Fig. 6 and the resulting $T_{\rm rot}$ and $Y_{\rm T}$ are given in Table 3 for sources "A" and "B". For source "A" the available single dish fluxes from the literature by van Dishoeck et al. (1995) have been overplotted, but have not been used for the fit. The single dish covers both components, but because the flux from source "A" is

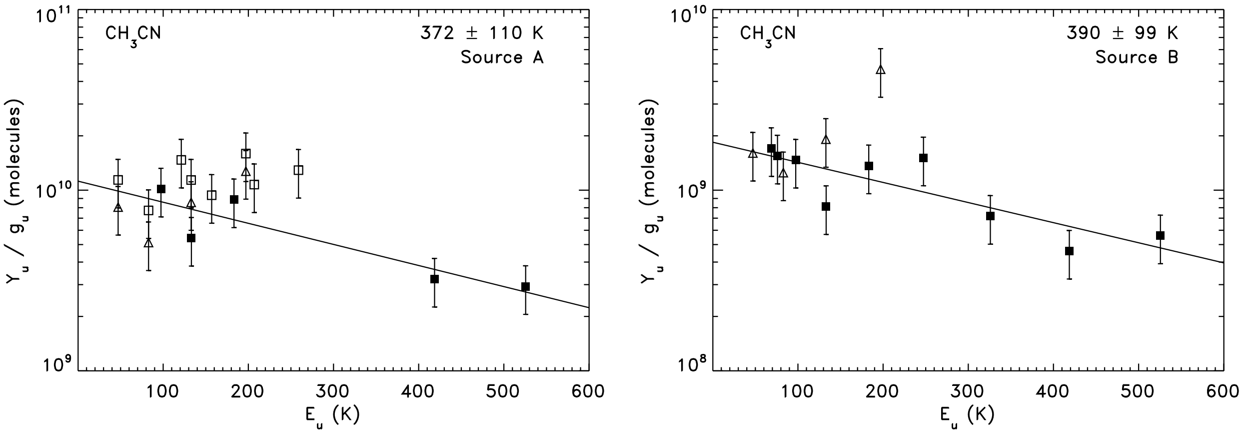

Fig. 7. Rotational diagram for CH_3CN transitions detected with the SMA shown as filled squares (■) toward IRAS 16293-2422 for source "A" (*left panel*) and source "B" (*right panel*). Emission lines detected with the JCMT observations by van Dishoeck et al. (1995) and the IRAM 30 m observations by Cazaux et al. (2003) are shown for source "A" with open squares (□). Emission lines detected by Bottinelli et al. (2004b) with the Plateau de Bure interferometer are shown for both sources with open triangles (△). Only the SMA data studied here is used for the fits. Uncertainties of 30% are over-plotted on the data.

significantly stronger than "B" (see Sect. 2.2), we assume that the single dish flux arises from source "A". The single dish fluxes are slightly larger than the fluxes from the SMA, also when the additional flux from the "B" source is taken into account. The rotational temperatures are the same for source "A" and "B", 277 ± 76 and 237 ± 56 K respectively, and much higher than what is detected by van Dishoeck et al. (1995) of 135 ± 40 K. This discrepancy is due to the fact that van Dishoeck et al. (1995) included lines in their fit which have rotational temperatures of only up to ~130 K, which results in a lower rotational temperature. Additionally, it is possible that extra flux in the single dish observations is due to extended emission from the larger scale envelope (see Sect. 3.1). The lines detected here range from 58 K to 447 K and have stronger constraints on the rotational temperature of compact HNCO emission. It is important to note that IRAS 16293-2422 emits at mid-infrared wavelengths (Jørgensen et al. 2005c), and thus infrared pumping of HNCO is possible. In that case the rotational temperature of HNCO is higher than the gas kinetic temperature – and thus than rotational temperatures determined for other molecules. When the model by Schöier et al. (2002) is used to fit the (u, v)-plot (see Fig. 5), the abundance of HNCO with respect to H_2 can be determined for the outer and inner envelope to be 6.0×10^{-11} and 4.0×10^{-9} assuming there is a jump in the abundance at 90 K. The inner abundance is somewhat uncertain, because the exact source size for the compact emission is not known.

For CH_3CN rotational diagrams are constructed for both sources (see Fig. 7). Less lines are usable for source "A" due to the larger line-width and line-blending. The single dish detections by van Dishoeck et al. (1995) and Cazaux et al. (2003) are over-plotted on the data for source "A" and are consistent with the SMA data within the uncertainties. For both sources the interferometric observations by Bottinelli et al. (2004b) with the Plateau de Bure interferometer have been over-plotted. These are also consistent with the SMA data, except for the 6_5–5_5 transition at 110.329 GHz with $E_u = 197$ K which is clearly too high for source "B". This may be due to line blending with the $CH_3^{13}CN$ 6_0–5_0 transition, which has a larger line strength than the main isotope. It is thus plausible that it contributes significantly to the line-flux. The resulting rotational temperatures are the same within the uncertainties for sources "A" and "B" (see Table 3). The transitions of the isotopomer $CH_3^{13}CN$ are unfortunately strongly blended in source "A" so that the determination of the optical depth is not possible. From the detections of lines for $CH_3^{13}CN$ for source "B" it is clear that the emission is optically thick and therefore that the resulting T_{rot} and Y_T from the rotational diagram of the main isotope are over- and underestimated, respectively (see Sect. 2.2). A rotational diagram has been constructed for source "B" from the four $CH_3^{13}CN$ lines and is shown in Fig. 8. The results of this fit are not well constrained because they are relatively close in excitation energy. However, the line intensities of the two highest excitation CH_3CN transitions, which are likely optically thin, can be added. When they are corrected for the $^{12}C/^{13}C$ isotopic ratio of 77 Wilson & Rood (1994), they are consistent with the fit and thereby decrease the uncertainty from 261 ± 485 K to 221±51 K (see Fig. 8). Using the value of $T_{rot} = 261$ K we can derive a number of molecules for CH_3CN for source B (see Table 3). For CH_3CN no extended emission can be inferred from the (u, v)-data. The lowest detected emission line has $E_u = 69$ K in our SMA data. Hence we cannot exclude the presence of extended emission for lines with even lower excitation energies.

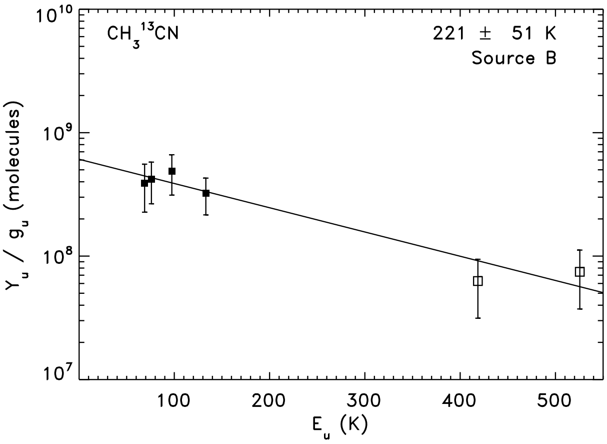

Fig. 8. Rotational diagram for $CH_3^{13}CN$ emission detected with the SMA toward source IRAS 16293-2422B shown as filled squares (■) and high excitation lines of the main isotope CH_3CN corrected for the $^{12}C/^{13}C$ isotopic ratio are shown as open squares (□). Uncertainties are over-plotted on the data.

4.2. CH_2CO, CH_3CHO and C_2H_5OH

CH_2CO has previously been detected by van Dishoeck et al. (1995) who found only very weak lines with the JCMT and CSO. Their derived rotational temperature is 35 K and column density 4×10^{13} cm^{-2}. Furthermore, Kuan et al. (2004) detected the CH_2CO $17_{2,15}$−$16_{2,14}$ transition at 343.694 GHz (E_u = 200 K) only toward source "B", suggesting that hot CH_2CO is also present. The $11_{1,11}$−$10_{1,10}$ transition (E_u = 76 K) detected here has a similar strength in both sources. A comparison with the single dish fluxes from van Dishoeck et al. (1995) shows that the SMA flux is lower by about a factor of 2. This may indicate that large scale emission from CH_2CO is resolved out with the SMA, consistent with the low rotational temperatures found in single-dish data (van Dishoeck et al. 1995). Unfortunately, it is difficult to derive the presence of extended emission from the (u, v)-visibility plots for the SMA observations, because the line strengths in sources "A" and "B" are so similar. Future higher angular resolution observations are needed to resolve this issue. Since only one line is detected for both CH_2CO and C_2H_5OH, it is not possible to determine rotational temperatures. Y_T can however be estimated when one assumes that CH_2CO and C_2H_5OH have the same rotational temperature as CH_3CHO.

Figure 9 shows the rotational diagram of the CH_3CHO lines detected with the SMA and the resulting values for T_{rot}, Y_T and the abundance x_{HNCO} with respect to HNCO are given in Table 3. Both CH_3CHO-A and CH_3CHO-E lines have been included in the fit with the assumption that their abundance ratio is unity and they both trace the same temperature gas. However, the result is not strongly influenced by this assumption since the fit to both CH_3CHO-A and E lines is within the uncertainties identical to the fit obtained to CH_3CHO-A lines only. The single dish data by Cazaux et al. (2003) are over-plotted on the rotational diagram but are not used for the fit. They are consistent with the SMA fluxes for $E_u > 50$ K. The rotational temperature calculated from the SMA data is 281±47 K. Cazaux et al. (2003) find a rotational temperature of ≤40 K, and furthermore their lower excitation lines lie significantly above the fit to the rotational diagram. This implies that the emission with $E_u < 30$ K originates from cold extended material. This is also consistent with interferometric observations of CH_3CHO in the high-mass star forming region Sgr B2(N) (Liu 2005), where the CH_3CHO emission is largely extended. The limit to the CH_3CHO/CH_3OH abundance ratio in source "A" is an order of magnitude lower than the detection in source "B", resulting both from a lower CH_3CHO and a higher CH_3OH column.

Previously, van Dishoeck et al. (1995) suggested that C_2H_5OH could be present in the spectra of this source, but were not able to make a firm identification based on strong line-blends. Huang et al. (2005) made the first conclusive detection of compact emission for C_2H_5OH toward source "A" for the $20_{3,17}$−$19_{3,16}$ transition at 354.757 GHz with E_u = 249 K. The detection here seems secure, but is blended with other lines (see Sect. 2.2). The previous detection by Huang et al. (2005) gives additional weight to the assignment of C_2H_5OH.

The emission of CH_2CO, CH_3CHO and C_2H_5OH behaves spatially very differently, also with respect to HNCO and CH_3CN. CH_2CO has emission that is similar in strength for sources "A" and "B" and for C_2H_5OH this also appears to be the case even though due to line blending it is not possible to determine this with certainty. However, the limit on Y_T for CH_3CHO is an order of magnitude lower than the detection toward source "B". The emission from CH_2CO and C_2H_5OH may arise from similar regions, but more transitions are required for a determination of the rotational temperatures.

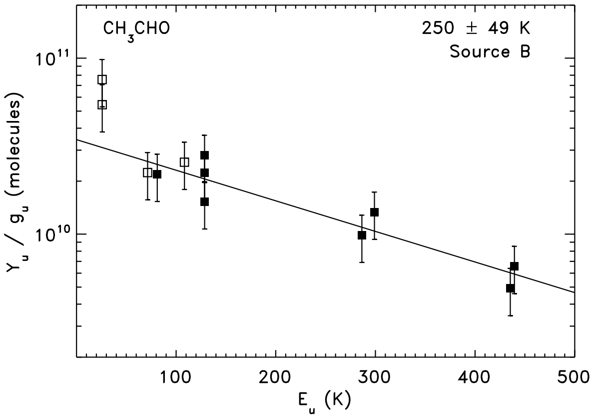

Fig. 9. Rotational diagram for CH_3CHO emission detected with the SMA toward source IRAS 16293-2422B shown as filled squares (■). The IRAM 30 m single dish data by Cazaux et al. (2003) are shown as open squares (□), but are not used for the fit. Uncertainties of 30% are over-plotted on the data.

5. Discussion

In this section the chemical implications of the observations are discussed. To compare the abundances of the species studied here with other sources, they are determined relative to the CH_3OH observations by Kuan et al. (2004) with the SMA (see Table 4). The value of Y_T has been calculated for CH_3OH from the integrated flux given by Kuan et al. (2004) assuming that the emission comes from a compact region with an average temperature of 200 K, a typical value found for the species in this study. The abundances are presented for individual components and the sum of "A + B" from the SMA data as well as previously published single dish results for IRAS 16293-2422 (van Dishoeck et al. 1995), the high-mass Orion hot core (Sutton et al. 1985) and the average over a survey of seven high-mass YSOs (Bisschop et al. 2007b). CH_3OH is taken as a reference molecule because it is one of the most abundant grain-surface products. Ideally, one would like to calculate the molecular abundances with respect to H_2 for the most direct comparison to chemical models. However, no accurate measure of the number of H_2 molecules exist: the dust continuum emission at (sub)millimeter wavelengths observed by interferometers is a combination of emission from both the circum-binary envelope and the emission from each of the compact disks around sources "A" and "B" (e.g., Schöier et al. 2004). Likewise, models for the larger-scale circum-binary envelope (e.g., Ceccarelli et al. 2000; Schöier et al. 2002) have typically been 1-dimensional and thus not meaningful for comparison of the relative abundances toward sources "A" and "B". The uncertainties in the number of molecules for CH_3OH lead to a possible error of −40% to +70% in the absolute abundance ratios in Table 4. For all molecules at the same position ("A" or "B") it is only ~30%.

5.1. HNCO and CH_3CN

It is striking that even though the line-widths of HNCO and CH_3CN are significantly different between the "A" and "B" components, their excitation and distribution is similar. When optical depth is taken into account it is very probable that both species are present in a similar environment.

Table 4. Comparison of IRAS 16293-2422 the abundances for source "A" and "B" normalized to the number of molecules of CH_3OH with those of other high-mass sources.

Molecule[a]	"A"	"B"	"A" + "B"	Single Dish[b]	Orion KL hot core[c]	High-mass survey[d]
HNCO	0.03	0.005	0.02	0.04	0.01	0.02
CH_3CN	>0.02	0.07	>0.02	0.04	0.04	0.08
CH_2CO	0.02	0.03	0.02	0.04	0.01	<0.005[e]
CH_3CHO	<0.0007	0.02	<0.007	<0.02	–	<0.003[e]
C_2H_5OH	–	0.01	–	≤0.05	–	0.025
H_2CO	–	–	–	0.24	0.1	0.22

[a] From Kuan et al. (2004), assuming the flux arises from a compact region with an excitation temperature of 200 K, [b] van Dishoeck et al. (1995), [c] Sutton et al. (1985), [d] Bisschop et al. (2007b), [e] limits determined from highest excitation lines detected for CH_2CO and CH_3CHO in the high-mass YSO survey by Bisschop et al. (2007b) assuming the emission comes from hot gas with $T_{\rm rot}$ = 200 K. Since much lower rotational temperatures have actually been determined the values indicate upper limits only.

Since HNCO and CH_3CN are nitrogen-bearing species their relative abundances compared to CH_3OH are not expected to be constant. However, it is interesting to note that the abundance ratios found for the low-mass IRAS 16293-2422 source as a whole ("A" + "B") are very similar to the Orion hot core (Sutton et al. 1985) and a high-mass survey (Bisschop et al. 2007b). Specifically, HNCO/CH_3OH is 0.02 for "A" and CH_3CN/CH_3OH is >0.02, to be compared with 0.01−0.02 and 0.04−0.08 for the high-mass sources, respectively. In contrast, for HNCO the differences between the two IRAS 16293-2422 sources "A" and "B" are larger than those with the high-mass sources. This suggests that both species are formed through the same mechanisms independent of cloud mass and luminosity, and that other factors cause the differences between individual objects.

The most likely formation mechanism for HNCO is OCN^- evaporation from grains (Allamandola et al. 1999; van Broekhuizen et al. 2004), whereas CH_3CN may partly form on the surfaces of grains from reactions of CH_3 with CN as well as in the gas phase from HCN with CH_3^+ (Garrod et al. 2008). One possible explanation for the large abundance difference between "A" and "B" is that the initial solid state abundances of nitrogen-bearing species such as OCN^- and NH_3 were higher in "A" than in "B", which resulted in higher gas phase HNCO abundance after evaporation. This may explain why the spatial distribution of HNCO is so different also from the oxygen-bearing species. Indeed the ice abundances of nitrogen-bearing species on grains vary strongly between different objects as is exemplified by the case of OCN^- for which variations of about an order of magnitude have been observed for sources that are only 400 AU apart (van Broekhuizen et al. 2005), similar to the distance between sources "A" and "B". Additionally, significant variations in the NH_3 ice abundance are seen in low-mass YSOs (Bottinelli et al., in prep.; Bottinelli et al. 2007a). Additionally, the gas phase abundance of $HC^{15}N$ is also almost an order of magnitude higher for source "A" compared to "B" Kuan et al. (2004), which suggests that the abundance of CH_3CN may also be enhanced in the gas phase.

5.2. CH_2CO, CH_3CHO and C_2H_5OH

A comparison of the abundances of CH_2CO, CH_3CHO and C_2H_5OH with respect to CH_3OH in hot gas with the SMA (Kuan et al. 2004) is given in Table 4. The hot CH_2CO and C_2H_5OH abundances relative to CH_3OH are similar to those found in high-mass sources. In contrast, the CH_3CHO abundance differs about a factor of ~30 between sources "A" and "B". This difference arises from the fact that the limit on the number of molecules for CH_3CHO is an order of magnitude lower toward source "A" compared to "B", whereas the number of molecules for CH_3OH is a factor of 2−3 higher toward source "A".

Tielens & Charnley (1997) explained the presence of these molecules through successive hydrogenation of HCCO, where complete hydrogenation leads to the formation of the most hydrogen-rich species C_2H_5OH and incomplete hydrogenation to one of the intermediate species CH_2CO and CH_3CHO. If hydrogenation of HCCO is the sole formation mechanism for all species there are three possible outcomes, (i) hydrogenation is complete; (ii) hydrogenation is incomplete or (iii) CH_3CHO is very efficiently converted to molecules other than C_2H_5OH at high temperatures in the ice or right after evaporation from the grain surface. For scenario (i) behavior such as observed for high-mass sources is expected with only C_2H_5OH seen in the hot gas, since CH_2CO and CH_3CHO are fully converted to C_2H_5OH. However, the detection of hot compact emission for CH_2CO and CH_3CHO implies that this cannot be the case. Thus it is possible that hydrogenation is incomplete (scenario ii). As demonstrated in the experiments by Bisschop et al. (2007a), the relative abundances of C_2H_5OH and CH_3CHO depend on time or rather on the total number of H-atoms the ice is exposed to. Additionally, the ice thickness affects the formation: for ices of a few monolayers thick some CH_3CHO molecules can be hidden from impinging H-atoms and this effect will depend strongly on ice morphology, such as porosity and the presence of other species in the ice. It then becomes difficult to predict the exact ratio between the relative abundances of CH_2CO, CH_3CHO and C_2H_5OH. This ratio may vary strongly per source.

One way to test scenario (ii) is to compare the abundance ratios C_2H_5OH/CH_3CHO and CH_3OH/H_2CO. These ratios are expected to be sensitive to the same ice morphology when grain-surface hydrogenation is the main formation mechanism. This is not an unreasonable assumption since H_2CO and CH_3OH were found to form through grain-surface hydrogenation from HCO in laboratory experiments (Watanabe et al. 2004; Fuchs et al. 2008). The CH_3OH/H_2CO abundance ratio is ~5 and in favor of CH_3OH, in contrast to 0.5 for the C_2H_5OH/CH_3CHO ratio toward source "B" which is in favor of CH_3CHO. It thus seems clear that there must be other processes than just the simple hydrogenation involved. However, since both the CH_2CO/CH_3OH ratio and C_2H_5OH/CH_3OH ratios are rather similar between different sources, it appears that it is mainly the chemistry of CH_3CHO that is not well understood.

Alternatively, CH_3CHO may be rapidly destroyed in the solid state or in the gas phase right after evaporation (scenario iii), while CH_2CO and C_2H_5OH are more stable. If this is correct, the determining factor for CH_3CHO destruction is absent or less strong for source "B" compared to "A". This could be an effect of e.g., UV-photolysis, although there is no a priori reason to expect very different photodissociation rates for these three species. The more quiescent nature of source "B" compared to "A" suggested by their different line widths could also play a role. Temperature effects are likely not important, since CH_3CHO has been detected with very high temperatures toward source "B". Alternatively, CH_3CHO and C_2H_5OH are not directly related. Further searches for CH_3CHO abundance variations compared to C_2H_5OH and CH_3OH are needed to elucidate its chemistry.

6. Summary and conclusions

We have performed an interferometric study of the complex organic species HNCO, CH_3CN, CH_2CO, CH_3CHO and C_2H_5OH toward the low-mass protostar IRAS 16293-2422 with the SMA. Previously published data from Kuan et al. (2004) are used to determine abundances relative to CH_3OH. The main conclusions of this work are:

- The emission from both HNCO and CH_3CN is compact and is seen toward both sources in the binary, with only 10−20% arising from source "B". Additionally, the lowest excitation line of HNCO shows extended emission suggestive of its presence in a cold extended envelope. The relatively higher abundances with respect to CH_3OH in source "A" may originate from higher initial abundances of OCN^- in the ice.
- For CH_2CO and C_2H_5OH only one line is detected due to compact emission. For CH_2CO these lines are detected with similar strength toward both sources and C_2H_5OH is clearly detected in source "B", but due to line-blending it is difficult to determine the flux for source "A". Compact hot emission for CH_3CHO is detected only toward source "B". Comparison with previous single dish observations by Cazaux et al. (2003) suggests that a cold extended component is present as well. If CH_2CO, CH_3CHO and C_2H_5OH are related through successive hydrogenation on the surfaces of grains, the same spatial behavior is expected for all three species. Since this is not observed, it suggests that hydrogenation reactions on grain surfaces alone cannot account for the observed gas phase abundance ratios. The difference between the two IRAS 16292-2422 sources can be explained if CH_3CHO would be selectively destroyed in source "A" right before or after grain-mantle evaporation.

The discussion in this paper demonstrates the strength of clearly resolved interferometric observations for studies of the chemistry in star forming regions. First, molecules that have both extended and compact emission can easily be identified based on (u, v)-visibility analysis. In single dish observations these components will be averaged together giving rotational temperatures in between that of the hot and cold component. Additionally, compact emission arising from different components in the same single-dish beam can be separated, which leads in some cases to abundance ratios that can vary over an order of magnitude for different sources as exemplified in Table 4 for HNCO and CH_3CHO. For HNCO the presence of a cold extended component could not be derived from the single dish observations, whereas for CH_3CHO it is the hot component that is not detected. Further interferometric studies are needed to elucidate the chemical relations between complex organics.

Acknowledgements. We thank Floris van der Tak and Xander Tielens for carefully reading this manuscript and an anonymous referee and the editor Malcolm Walmsley for constructive comments on the paper. Funding was provided by NOVA, the Netherlands Research School for Astronomy and a Spinoza grant from the Netherlands Organization for Scientific Research (NWO).

References

Adams, F. C., Lada, C. J., & Shu, F. H. 1987, ApJ, 312, 788
Allamandola, L. J., Bernstein, M. P., Sandford, S. A., & Walker, R. L. 1999, Space Sci. Rev., 90, 219
Bisschop, S. E., Fuchs, G. W., van Dishoeck, E. F., & Linnartz, H. 2007a, A&A, 474, 1061
Bisschop, S. E., Jørgensen, J. K., van Dishoeck, E. F., & de Wachter, E. B. M. 2007b, A&A, 465, 913
Blake, G. A., van Dishoeck, E. F., Jansen, D. J., Groesbeck, T. D., & Mundy, L. G. 1994, ApJ, 428, 680
Bottinelli, S., Ceccarelli, C., Lefloch, B., et al. 2004a, ApJ, 615, 354
Bottinelli, S., Ceccarelli, C., Neri, R., et al. 2004b, ApJ, 617, L69
Bottinelli, S., Boogert, A. C. A., van Dishoeck, E. F., et al. 2007a, in Molecules in Space and Laboratory, ed. J. L. Lemaire, & F. Combes (S. Diana)
Bottinelli, S., Ceccarelli, C., Williams, J. P., & Lefloch, B. 2007b, A&A, 463, 601
Cazaux, S., Tielens, A. G. G. M., Ceccarelli, C., et al. 2003, ApJ, 593, L51
Ceccarelli, C., Caux, E., Loinard, L., et al. 1999, A&A, 342, L21
Ceccarelli, C., Loinard, L., Castets, A., Tielens, A. G. G. M., & Caux, E. 2000, A&A, 357, L9
Chandler, C. J., Brogan, C. L., Shirley, Y. L., & Loinard, L. 2005, ApJ, 632, 371
Fuchs, G. W., Ioppolo, S., Bisschop, S. E., Van Dishoeck, E. F., & Linnartz, H. 2008, A&A, submitted
Garrod, R. T., Widicus Weaver, S. L., & Herbst, E. 2008, ApJ, 682, 283
Gibb, E. L., Whittet, D. C. B., Boogert, A. C. A., & Tielens, A. G. G. M. 2004, ApJS, 151, 35
Goldsmith, P. F., & Langer, W. D. 1999, ApJ, 517, 209
Huang, H.-C., Kuan, Y.-J., Charnley, S. B., et al. 2005, AdSpR, 36, 146
Ikeda, M., Ohishi, M., Nummelin, A., et al. 2001, ApJ, 560, 792
Ikeda, M., Ohishi, M., Nummelin, A., et al. 2002, ApJ, 571, 560
Jørgensen, J. K., Schöier, F. L., & van Dishoeck, E. F. 2002, A&A, 389, 908
Jørgensen, J. K., Bourke, T. L., Myers, P. C., et al. 2005a, ApJ, 632, 973
Jørgensen, J. K., Lahuis, F., Schöier, F. L., et al. 2005b, ApJ, 631, L77
Jørgensen, J. K., Schöier, F. L., & van Dishoeck, E. F. 2005c, A&A, 435, 177
Jørgensen, J. K., Bourke, T. L., Myers, P. C., et al. 2007, ApJ, 659, 479
Keane, J. V. 2001, Ph.D. Thesis, Rijks Universiteit Groningen
Kleiner, I., Lovas, F. J., & Godefroid, M. 1996, J. Phys. Chem. Ref. Data, 25, 1113
Kuan, Y.-J., Huang, H.-C., Charnley, S. B., et al. 2004, ApJ, 616, L27
Liu, S.-Y. 2005, in ed. D. C. Lis, G. A. Blake, & E. Herbst, IAU Symp., 231, 217
Mundy, L. G., Wootten, A., Wilking, B. A., Blake, G. A., & Sargent, A. I. 1992, ApJ, 385, 306
Nummelin, A., Bergman, P., Hjalmarson, Å., et al. 2000, ApJS, 128, 213
Olmi, L., Cesaroni, R., & Walmsley, C. M. 1993, A&A, 276, 489
Qi, C. 2006, The MIR Cookbook, The Submillimeter Array/Harvard Smithsonian Center for Astrophysics
Remijan, A. J., & Hollis, J. M. 2006, ApJ, 640, 842
Sakai, N., Sakai, T., & Yamamoto, S. 2006, PASJ, 58, L15
Sakai, N., Sakai, T., & Yamamoto, S. 2007, ApJ, 660, 363
Schöier, F. L., Jørgensen, J. K., van Dishoeck, E. F., & Blake, G. A. 2002, A&A, 390, 1001
Schöier, F. L., Jørgensen, J. K., van Dishoeck, E. F., & Blake, G. A. 2004, A&A, 418, 185
Shirley, Y. L., Evans, II, N. J., & Rawlings, J. M. C. 2002, ApJ, 575, 337
Sutton, E. C., Blake, G. A., Masson, C. R., & Phillips, T. G. 1985, ApJS, 58, 341
Takakuwa, S., Ohashi, N., Bourke, T. L., et al. 2007, ApJ, 662, 431
Tielens, A. G. G. M., & Charnley, S. B. 1997, Origins Life Evol. B., 27, 23
Turner, B. E. 1991, ApJS, 76, 617
van Broekhuizen, F. A., Keane, J. V., & Schutte, W. A. 2004, A&A, 415, 425
van Broekhuizen, F. A., Pontoppidan, K. M., Fraser, H. J., & van Dishoeck, E. F. 2005, A&A, 441, 249
van der Tak, F. F. S., van Dishoeck, E. F., & Caselli, P. 2000, A&A, 361, 327
van der Tak, F. F. S., Boonman, A. M. S., Braakman, R., & van Dishoeck, E. F. 2003, A&A, 412, 133
van Dishoeck, E. F., Blake, G. A., Jansen, D. J., & Groesbeck, T. D. 1995, ApJ, 447, 760
Watanabe, N., Nagaoka, A., Shiraki, T., & Kouchi, A. 2004, ApJ, 616, 638
Wilson, T. L., & Rood, R. 1994, ARA&A, 32, 191
Yeh, S. C. C., Hirano, N., Bourke, T. L., et al. 2008, ApJ, 675, 454
Zinchenko, I., Henkel, C., & Mao, R. Q. 2000, A&A, 361, 1079

Appendix A: SMA spectra

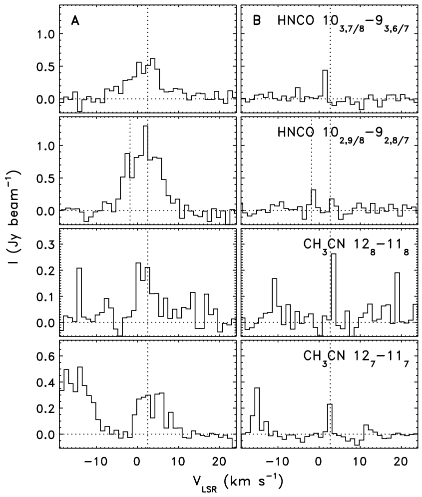

Fig. A.1. Individual SMA spectra for the $10_{3,7/8}-9_{3,6/7}$, $10_{2,9}-9_{2,8}$ and $10_{2,8}-9_{2,7}$ HNCO transitions and the 12_8-11_8 and 12_7-11_7 CH_3CN transitions. The spectra for the "A" position are depicted in the *left column* and for "B" in the *right column*. The vertical dotted line indicates the average systemic line position. The horizontal dotted line shows the baseline.

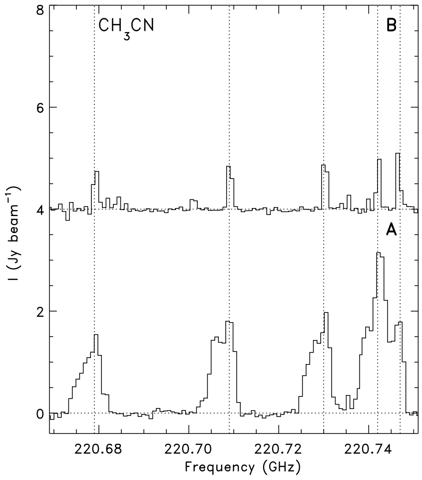

Fig. A.2. SMA spectrum in the 220.668–220.752 GHz range for sources "A" (*lower spectrum*) and "B" (*upper spectrum*). The vertical dotted lines indicate the positions of, from left to right, the 12_4-11_4, 12_3-11_3, 12_2-11_2, 12_1-11_1 and 12_0-11_0 CH_3CN transitions and the horizontal dotted lines the baseline.

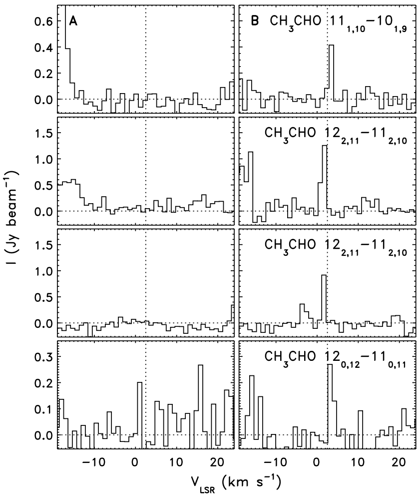

Fig. A.3. Individual SMA spectra for, from left to right, the $11_{1,10}-10_{1,9}$, $12_{2,11}-11_{2,10}$, $12_{2,11}-11_{2,10}$, $12_{0,12}-11_{0,11}$ and $12_{5,8/8}-11_{5,7/6}$ CH_3CHO-A transitions. The spectra for the "A" position are depicted in the *left column* and for "B" in the *right column*. The horizontal dotted line shows the baseline.

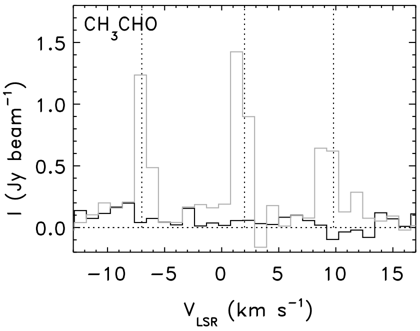

Fig. A.4. SMA spectra for the $12_{3,9}-11_{3,8}$, $12_{5,7}-11_{5,6}$, and $12_{5,8}-11_{5,7}$ CH_3CHO-E transitions (dotted lines). The black line indicates the emission spectrum toward "A" and the grey line toward "B". The horizontal dotted line shows the baseline.